Propeller influence on the aeroelastic stability of High Altitude Long Endurance aircraft

P.C. Teixeira[ID] **and C.E.S. Cesnik**[ID]
pct@umich.edu
Department of Aerospace Engineering
University of Michigan
Ann Arbor
MI
USA

ABSTRACT

This work investigates the propeller's influence on the stability of High Altitude Long Endurance aircraft, incorporating all resultant loads at the propeller hub, propeller slipstream, and gyroscopic loads. Such effects are usually neglected in the aeroelastic simulation of HALE aircraft. For that goal, a previously developed framework, which couples a geometrically nonlinear structural solver with an Unsteady Vortex Lattice method (uVLM) for lifting surfaces and a Viscous Vortex Particle (VVP) method for propeller slipstream, was employed to generate time-data series. Also, a method, based on a combination of Proper Orthogonal Decomposition and system identification, to extract dynamic information (frequencies, damping, and modes) of the aircraft from a time-series signal is proposed and successfully tested for a purely structural case, for which reference data is available. The method is then applied to investigate the stability of aeroelastic cases. The results demonstrate that the presence of propellers can influence the aeroelastic stability of a Very Flexible Aircraft.

1.0 INTRODUCTION

In recent decades a new concept of unmanned air vehicle (UAV) has received increased attention due to its low energy consumption and promising applications: High-Altitude Long Endurance (HALE) aircraft. In order to achieve their higher aerodynamic performance, HALE aircraft are typically high-aspect-ratio configurations, resulting in a very flexible structure, which imposes additional challenges to aircraft stability and control. Also, due to the typical low cruise speed, a propeller-motor combination is often the choice of propulsion.

The presence of propellers results in different kinds of loads transmitted to an aircraft:

(i) aerodynamics loads, composed of the resultant loads acting on the propeller hub (thrust, side and normal forces, torque, and yaw/pitching moments due to asymmetric blade loading, known as P-factor) and the influence of propeller slipstream on lift distribution of surfaces behind the propeller, and;

(ii) inertial loads, which include the inertial effects due to propeller CG acceleration and the gyroscopic moments due to the variation of blades angular momentum when the aircraft performs a yaw or pitch motion.

Despite those different loads, in the context of very flexible aircraft the modeling of propeller effects is usually reduced to just a concentrated force (thrust), and little has been explored about the influence of the other propeller effects on the aeroelastic stability of such very flexible structures.

1.1 Propeller influence on flight dynamics stability

Early studies associated with the modeling and investigation of propeller effects in aircraft stability date from the first decades of the twentieth century. In Lanchester[1], from 1917, a whole appendix is dedicated to notes about the effects of propulsion on a flying machine. Harris[2] develops a mathematical formulation for side forces acting on a propeller as a response to yaw and Glauert[3,4] extends that formulation to derive other stability derivatives associated with the propeller.

Following those early investigations, in the work of Katzoff[5], experimental data obtained on the NACA full-scale wind tunnel for eight different aircraft configurations were investigated in terms of the effects of the propeller in longitudinal stability and control. Among the conclusions, it was noticed that the loss of elevator effectiveness at high angles of attack can be largely eliminated by the inclusion of propeller. Also, the rate of increase of effective downwash angle with the angle-of-attack can be considerably increased due to the influence of propellers for certain aircraft configurations, as gull-wing and parasol-wing monoplanes. Ribner[6] extended some previous formulations to determine the side force of propeller due to yaw by incorporating induction effects and determines an expression for the side forces based on an analogy with fins, with the effective fin area taken as the lateral projected area of the propeller plane. It was observed that besides the side force, a single propeller in yaw also experiences a pitching moment. A dual-rotating propeller develops up to one-third more side force than a single one. Also, the side forces due to angular velocities of pitch or yaw were found to be negligible for typical angular velocities that can be realised in maneuvers, with the exception of spin.

In Butler et al, the slipstream effects in a v/stol aircraft performance and stability were studied. For that, an analytical investigation was proposed and correlated to experimental data. Following a performance investigation, a study on the slipstream influence on stability and control characteristics, as well the feasibility of use slipstream for stability augmentation. Preliminary results indicated that slipstream can be used as a potential solution for improving the dynamic stability of a tilt-wing aircraft in hovering flight.

Although one century has passed since the early studies, due to the complexity of the problem and new tools available, the investigation and modeling of propeller influence on aircraft stability are in continuous progress in recent years. Some examples of more recent efforts in this topic are the works of Jamison[7], Goraj and Cichocka[8] and Bouquet[9]. In Jamison[7], flight tests were performed with the E-2C aircraft for two different propeller models, Hamilton-Sundstrand model 54460-1 and model NP2000. The results pointed out that substituting one propeller by the other, with all other test conditions kept the same, influences the static longitudinal aircraft stability significantly.

Goraj and Cichocka[8] studied the influence of gyroscopic effects on the stability of a light aircraft. Two types of gyroscopic effects were distinguished: weak gyroscopic effects, corresponding to maneuvers with small changes in pitch and yaw rates (classical dynamic

stability), and strong gyroscopic effects, corresponding to rapid manoeuvres, with substantial pitching and yaw rates. In this last case, it was found that coupling between lateral and longitudinal degrees of freedom can be significant, potentially causing loss of control.

The influence of propeller slipstream is investigated in the work of Bouquet[9], whose focus was developing, implement, and validate a prediction method for the effects of the propeller on longitudinal stability. The implemented approach is based on Obert's method, which was found to be computationally inexpensive and with relatively accurate results. It was observed four major effects caused by propeller slipstream: on the longitudinal stability: an additional normal force at propeller disk, the influence of slipstream on the wing, influence in tail-off pitching moment, and change in tail contribution to the pitching moment. In the case of Fokker 50, It was found a decrease in tail effectiveness due to an increase in the downwash angle at the tail with the presence of propellers.

1.2 Propeller influence on aeroelastic stability

1.2.1 Linear regime

Studies of other propeller effects besides thrust on the aeroelastic stability have been limited to problems involving displacements inside the linear regime, as in Rezaeian[10], Sui An[11] and Guruswamy[12].

In Rezaeian[10], a numerical investigation of the two main instability phenomena associated with a propeller-nacelle-wing system was performed using the software ZAERO. The influence of propeller on modal damping was studied, including slipstream and gyroscopic modeling. It was observed that gyroscopic effects had influenced the modal damping of the wind tunnel wing.

The development of a gradient-based aeroelastic optimisation considering propeller influence is presented in Sui An[11]. The framework employs the Double Lattice method for surfaces aerodynamics, actuator disk to model the average effects of the propeller (one-way coupling), and uses the Toolkit for the Analysis of Composite Structures (TACS) for the structural analysis. Results indicated that despite the improvement expected for aerodynamic efficiency, an increase in aspect ratio and the number of propellers can make the structure more vulnerable to instabilities and structural failures. The effect back of wing on propellers, the gyroscopic moments, and the nonlinearities for structure and aerodynamics were not included in that model. Also, aeroelastic static and dynamic considerations (in terms of elastic and rigid body displacements) were not the focus of that investigation.

In recent work, Guruswamy[12] investigated the influence of a wingtip mounted propeller on the aeroelastic stability of a flexible aircraft with aspect ratio five. The flow-field is simulated based on Navier–Stokes equations, while the structure is modeled using plate finite elements. Results for the wing model with and without the tip propeller showed that propeller caused destabilising effects for the same freestream condition. However, increasing the propeller RPM, a stable response could be achieved.

1.2.2 Nonlinear regime

In the context of very flexible aircraft, which are characterised by a highly nonlinear behavior, the investigations of propeller effects on the aeroelastic stability have been limited to cases with thrust only.

Previous works like Hodges et al[13], Feldt and Herrmann[14] and Quanlong et al[15] have demonstrated that follower thrust has an important influence on the aeroelastic stability.

In Hodges et al[13], the effects of thrust on the bending-torsion flutter of very flexible wings were investigated. For this purpose, the thrust was modeled as a follower force with a prescribed magnitude. Propeller gyroscopic and slipstream effects were not included. A nonlinear mixed finite element method was used to the structural model of the wing, represented by beams, and a finite-state two-dimensional unsteady aerodynamic approach was used to model wing aerodynamics. Their results suggest that thrust has either a stabilising or destabilising effect depending on the ratio, λ, of bending stiffness to torsional stiffness. If $\lambda < 5$, it was observed that an increase in thrust, up to a certain value, increases the flutter speed. For $\lambda > 10$, thrust contributes to decreasing flutter speed. Differences up to 11% in flutter speed were observed, pointing to the importance of considering engine thrust influence on wing flutter of very flexible aircraft. While the thrust as a follower force can be included in the analysis relatively easily, the lack of propeller aerodynamic and inertial effects on the free flight of very flexible aircraft may be a potential source of errors in simulations.

In Feldt and Herrmann[14], the bending-torsional flutter of a cantilevered wing with a lumped mass on its tip was investigated. It was found that the follower forces contributed to reducing the critical speed, while an increase in the tip mass demonstrated a stabilising effect. Quanlong et al[15] also concluded that the presence of thrust, modeled as a follower force, reduces the flutter limit. In the case considered, a reduction of flutter speed in more than 10% was noted.

1.3 Propeller modeling on nonlinear aeroelastic frameworks

Due to its large deflections under typical loads conditions, VFA is characterised by nonlinear behavior. However, traditional aeroelastic frameworks make use of linear theory for structural and aerodynamics formulations[16].

Separate research group efforts have developed aeroelastic framework capable of taking into account the nonlinear aspects of the VFA behavior. Examples of state of the art codes in this context cited on literature are UM/NAST[17,18,19] from University of Michigan, SHARPy[20,21,22,23] from London Imperial College, ASWING[24,25,26] from Massachusetts Institute of Technology, NATASHA[27,28], from Georgia Institute of Technology, and DLR toolbox[29,30], from Deutsches Zentrum für Luft-und Raumfahrt (DLR).

Concerning the modeling of the propeller effects, usually the aeroelastic frameworks for VFA consider the thrust effect only, modeled as a follower punctual force. Exceptions are, from the best of the authors' knowledge, for ASWING and the current version of UM/NAST.

ASWING employs an actuator disk model and can model thrust, torque and P-factor loads (loads due to asymmetric loading of blades)[25,26].

UM/NAST originally also incorporated just thrust to model the propeller effects. However, developments made by previous works of the authors[31,32,33] made possible the complete inclusion of the propeller effects in a nonlinear aeroelastic framework (composed of all the resultant aerodynamic loads on the hub, the aerodynamic effects of propeller slipstream, and its inertial effects). The unsteady aerodynamics is based on Lifting Line plus Viscous Vortex Particle method for the propellers combined with an Unsteady Vortex Lattice for the lifting surfaces, allowing it to capture propwash effects as well as the interaction of the flow among multiple lifting surfaces. Also presented there is the derivation of the inertial loads associated with the rotating blades and the procedure for the integration of the different involved approaches. Such previous works focused on the development of the framework itself and in the analysis of how the propeller effects impacted static and dynamic simulations of VFA. Investigations on aeroelastic stability were not performed.

1.4 Paper objectives and organization

From the previous sections, one can conclude that although many studies with rigid configurations have demonstrated that propellers can significantly influence an aircraft performance and flight dynamics stability, few investigations have been conducted on the effects of propellers on the aeroelastic stability of very flexible aircraft. Moreover, state-of-the-art nonlinear coupled aeroelastic-flight dynamics frameworks for very flexible configurations usually lack complete modeling of propeller effects, and just the thrust is typically included.

In view of such issues, this paper has the following goals:

(i) Investigate the impact of propeller effects on the aeroelastic stability of VFA;
(ii) Get insight on the isolated contribution of the different kinds of loads transmitted by the propeller.

To accomplish these objectives, an enhanced aeroelastic framework developed in previous works by the authors[31,32,33], and capable of incorporating the different propeller effects, is employed to generate snapshots data for a HALE aircraft model with propellers. Also, a method to extract frequencies, damping, and modes from time-series data, based on a combination of Proper Orthogonal Decomposition (POD) and system identification (sys ID), is proposed and verified for a purely structural case, for which reference data is available.

The remaining of this paper is organised as follows: Section 2 describes key aspects of the enhanced aeroelastic framework with propellers previously developed by the authors[31,32,33]. Section 3 describes the motivation and strategy of an alternative approach to extract dynamic information from simulations of VFA with propellers. The method is then verified and applied for numerical investigations in Section 4. Finally, concluding remarks and key contributions of this work are summarised in Section 5.

2.0 AEROELASTIC FRAMEWORK WITH PROPELLER

The point of departure for the aeroelastic framework used in this work is the University of Michigan's Nonlinear Aeroelastic Simulation Toolbox (UM/NAST)[17,18,19]. UM/NAST is a multidisciplinary tool developed for the simulation of very flexible aircraft. It features solutions for the modal characterisation about different steady state conditions, static, trim, and nonlinear transient simulations and aeroelastic stability analyses. For that, the equations for structural dynamics, nonlinear 6-DoF vehicle dynamics and aerodynamics are solved simultaneously.

In order to take into account the different propeller effects, the original UM/NAST framework was enhanced, as described in previous works by the authors[31,32,33], with an Unsteady Vortex Lattice for the lifting surfaces and a Lifting Line and Viscous Vortex Particle (LL/VVP) methods to model the propeller aerodynamics. Furthermore, inertia effects associated with the rigid rotating blades were also incorporated.

Figure 1 presents an overview of the enhanced coupled aeroelastic-flight dynamics framework, for the case of dynamic simulation. For each time step, based on current values of loads and control inputs, the new geometric configuration of the structure is determined. Beam coordinate deformations are then converted to panel grid point deformations, and aerodynamic loads are calculated with uVLM coupled to LL/VVP. Those loads are converted to concentrated loads at beam nodes, and the dynamic process continues until the predetermined simulation time is reached. It is important to note that the contribution of the elastic deformation of the body in the effective free-stream speed is considered in both uVLM and LL/VVPs.
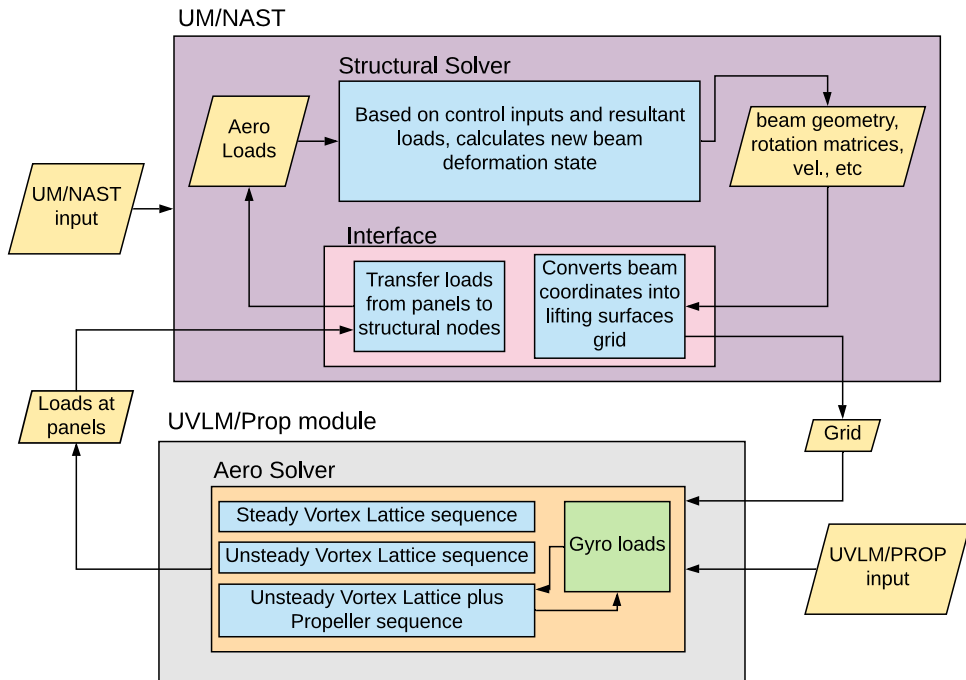
Figure 1. Enhanced coupled aeroelastic-flight dynamics framework with propeller effects.

In the next sections, key aspects of the various components of this framework are described, focusing on the parts added by the authors in previous works[31,32,33]. For more details about the formulation, numerical implementation, as well as verification cases of the different parts included, the reader can report to Refs (33,34).

2.1 Structural model

The structural model is based on a geometrically nonlinear formulation using a strain-based nonlinear finite element model of Su and Cesnik[35]. In this approach, constant strain in extension, twist, and in- and out-of-plane bending is assumed inside each beam element. Nonlinear equations of motion are also solved in terms of those strain values, and the related displacements are post-processed.

2.2 Lifting surfaces aerodynamics

The original aerodynamic modeling in UM/NAST framework employed a corrected strip theory based on Peters' inflow theory[36,37]. However, as concluded in the investigation performed by Ritter et al[38], although strip theory has been a popular method for the aeroelastic simulation of very flexible aircraft[13,18,17,39,40,41,42], its inability to take into account mutual lifting surfaces influence and other 3D effects limit its accuracy and the possible range of applications. In order to capture the interaction of propellers and aircraft lifting surfaces, a method capable of taking into account that mutual aerodynamic influence was necessary. For that purpose, the Unsteady Vortex Lattice method (UVLM) was selected, and a UVLM code developed by Ritter[43] was adapted and integrated to UM/NAST framework, as an additional aerodynamic option.

Vortex Lattice has the advantage to be capable of modeling the aircraft undergoing large translations and rotations and has become a popular method in aeroelastic frameworks for the simulation of VFA[38,20,44,45,46,47,48,49,50]. Also, for conditions within the limitations and assumptions considered in its formulation, Vortex Lattice results demonstrate remarkable agreement with CFD and experimental data[51,52,53]. Its range of validity is typically the case of very flexible aircraft, whose usual velocities are within the incompressible regime, but with high enough Reynolds number to assume that the viscous effects are confined in a thin boundary layer.

Assuming potential flow and applying vortex ring elements distributed along panels and wake panels of lifting surfaces, the circulation at each panel is solved satisfying the no-penetration boundary condition:

$$[AIC]\,\Gamma = -u_n, \qquad \qquad \dots (1)$$

where $[AIC]$ is the aerodynamic influence coefficient matrix (which gives influence of one panel on another one), Γ is the vector of circulation at each panel, and u_n represents the normal component of total velocity at panel's control points due to free-stream, body elastic deformation, mutual influence between panels, influence of the wake and any other influence of velocity field, as the presence of the propeller slipstream.

The wake is updated using a time-stepping approach. In this work, although any influence on the velocity flow field can be included, just the onflow velocity (velocity due to rigid body motion and atmospheric perturbation) was considered for the wake convection. This reduces the computational cost (and possible numerical instabilities related to wake roll-up) while still retaining enough information to capture wake-surfaces interaction. Also, it was observed in simulations of representative VFA that the effects of wake roll-up are usually not significant[54,55].

Also, induced and profile drags are included. In order to estimate the profile drag, the local lift coefficient, c_l, of each strip is first calculated. Then, the corresponding drag coefficient, c_d, is determined based on a polar table (e.g. XFOIL), matching the local value of c_l with the corresponding value of c_d. Rotation matrices based on UM/NAST formulation are used to rotate forces from wind axis to body system for each deformed configuration.

2.3 Propeller blade aerodynamics

In this work, the Lifting Line (LL) approach was chosen for the blades aerodynamics due to its simplicity, small computational cost, and good capability to represent unsteady behaviour of blade circulation, as observed in Abedi et al[56]. It should be noted that, in this context, LL is applied to model the bound vorticity only and will be coupled to another approach for the wake model, as will be discussed soon.

For each section, the local blade twist (β), chord, aerofoil type, and associated polar tables (for a range of Reynolds number and angle-of-attack) are provided. In this work, data from XFOIL was used to generate the polar tables, but any other data source, such as experiment or CFD, could be used as well. XFOIL employs the e^N method for transition prediction, which depends on the choice of the parameter N_{crit}, corresponding to the amplification factor of the most amplified frequency that causes the transition. The default value is 9, and it was applied in this work unless otherwise stated.

At each time step, based on the local flow velocity, the sectional Reynolds number and effective angle-of-attack, α, are calculated and used to interpolate the local aerodynamic

coefficients, c_l, c_d and c_m from the polar tables provided. The loads at each section are then calculated (using the component of total velocity aligned with the section), and the resultant loads acting on the propeller hub can be determined. Those loads are then transferred to the structural nodes where the propellers are attached.

The bound vortex segments circulation is calculated from the combination of 2D Kutta–Jukowski theory and the definition of lift coefficient:

$$\Gamma = 1/2cV_{\text{section}}c_l \qquad \qquad \dots (2)$$

where Γ is the circulation at the considered control point, c is the local chord, V_{section} is the component of total velocity at the control point that is in the plane of aerofoil section considered, and c_l is the local lift coefficient.

2.4 Propeller wake aerodynamics

There are many possibilities of propeller wake modeling available on literature, ranging from high-cost, high-fidelity solutions, as CFD approaches, to low-cost, low-fidelity solutions, as Momentum Theory, vortex filaments or panels (prescribed and free-wake), and semi-empirical approaches.

While CFD can be used to capture complex effects, as viscous effects, dynamic stall, and flow separation, and has demonstrated good capability to reproduce experimental results, it is usually too expensive, in particular in the case of multiple surfaces and propellers.

On the other hand, although the lower-fidelity approaches provide a much quicker evaluation of propeller slipstream velocities, their accuracy is limited: many of them assume a pre-determined wake shape, isolated propeller configuration, and usually capture just averaged effects. Although those methods can be enough for some applications, this is not the case of a dynamically deforming VFA, which may contain multiple surfaces and propellers.

2.4.1 Viscous Vortex Particle

A promising alternative to those methods is the Viscous Vortex Particle method (VVP), a mid-fidelity approach that is able to capture unsteady wake behaviour, viscous diffusion, vortex mixing, and decay, as well as complex wake-wake and wake-lifting surfaces interactions, showing a good correlation with CFD and experimental results[57,58,59], but at a much smaller cost than CFD, yet higher than low-fidelity solutions. Instead of applying numerical discretisation over the entire flow-field, as is typically done in CFD formulations, the method directly solves the vorticity-velocity form of incompressible Navier–Stokes equations with a Lagrangian formulation, resulting in a grid-free modeling of wake diffusion without problems of artificial numerical dissipation. Also, due to the vorticity representation of the flow by free vortex particles, they can move freely with local flow velocity, allowing a natural development of the wake and avoiding singularities due to intersections between wake and lifting surfaces. Additionally, the Viscous Vortex Particle method has been successfully applied in many studies involving rotors and propellers and their interaction with other lifting surfaces or propellers[58,60,59,61,62,63,64].

A point of concern in VVP is that for N particles, it has a characteristic speed of $O(N^2)$. Then, as the number of particles increases with time, the computational cost increases significantly, and some acceleration procedure may be necessary. In this work, a cut-off distance is applied when particles are sufficiently far away from the region of interest. The sensitivity of

the Viscous Vortex Particle simulation to the choice of cut-off distance was investigated by He and Zhao[59] for a rotor model. For that case, it was concluded that the influence of the wake cut-off distance (r_{cut}) on the simulation results is not significant, provided that $r_{cut} \geq 2R$.

In the next section, key aspects of the VVP are presented. For more in-depth details about the VVP the reader is referred to Winckelmans and Leonard[65].

2.4.2 Basic equation and assumptions

In the VVP, both viscosity and rotational effects are taken into account. The assumption of incompressible flow, however, is retained. From the classical Navier–Stokes equations for incompressible flow, the momentum conservation for a differential fluid element is:

$$\frac{\partial \vec{u}}{\partial t} + (\vec{u} \cdot \nabla)\,\vec{u} = -\frac{1}{\rho}\nabla p + \nu \nabla^2 \vec{u}, \qquad \dots (3)$$

where $\vec{u}(\vec{x}, t)$ is the velocity field, $\omega(\vec{x}, t)$ is the vorticity field, $p(\vec{x}, t)$ is the pressure field and ρ and ν are the fluid density and kinematic viscosity, respectively.

Taking the curl of Equation (3), using the fact that the fluid is incompressible (then, from continuity equation, $\nabla \cdot \vec{u} = 0$) and remembering the definition of vorticity, ($\omega = \nabla \times \vec{u}$), Equation (3) can be re-written as:

$$\frac{D\vec{\omega}}{dt} = [\vec{\omega} \cdot \nabla]\vec{u} + \nu \nabla^2 \vec{\omega}, \qquad \dots (4)$$

where $D()/dt = \partial()/\partial t + \vec{u} \cdot \nabla()$ is the material derivative.

Equation (4) is the vorticity-velocity in the Lagrangian form, and it is the fundamental equation for solving the transport of vorticity in the VVP.

2.4.3 Vorticity field discretization

The key idea behind the VVP is that the vorticity field can be discretised into vortex particles, corresponding to influencing elements characterised by a volume, a position, and strength. The global vorticity field is then approximated by the sum of each particle's individual vorticity field.

In the classical proposition of the Vortex Particle method, the vorticity field is assumed to be concentrated at discrete points, called singular particle or point vortex[65,66] and can be written as:

$$\vec{\omega}(\vec{x}, t) = \sum_{i=1}^{N} \delta(\vec{x} - \vec{x}_i)\vec{\alpha}_i(t), \qquad \dots (5)$$

where $\delta(x)$ is the 3D δ-function, and $\vec{x}_i$ is the particle position and $\vec{\alpha}_i$ corresponds to its strength, which is given by the particle volume times the vorticity, $\vec{\alpha}_i = \vec{\omega}_i vol_p$. Then, in this approach, the region outside of the vortex particles is irrotational.

The velocity field associated with such particles representation can be demonstrated[65] to be:

$$\vec{u}_\Psi(\vec{x}, t) = \nabla \times \vec{\Psi}(\vec{x}, t) = \sum_{i=1}^{N} \vec{K}(\vec{x} - \vec{x}_i) \times \vec{\alpha}_i(t), \qquad \dots (6)$$

where $\vec{K}(\vec{x} - \vec{x}_i)$ is the Biot–Savart kernel, given by:

$$\vec{K}(\vec{x} - \vec{x}_i) = -\frac{1}{4\pi} \frac{\vec{x} - \vec{x}_i}{|\vec{x} - \vec{x}_i|^3} \qquad \ldots (7)$$

From a quick examination of the Biot–Savart kernel, one can conclude that it is a singular function, leading to numerical instabilities when particles move toward each other. To overcome this problem, the concept of "regularised particles," also known as "vortex blob" was introduced[67] and is widely applied by studies using VVP.

The basic idea of regularised particles is to substitute the 3D δ-function, $\delta(\vec{x} - \vec{x}_i)$, in the vorticity field representation (Equation (5)) by a distribution function (known as regularisation function, regularised smoothing kernel or also cutoff function), $\xi_\sigma(\vec{x} - \vec{x}_i)$, such that the point vortex particles are transformed into vortex "blobs'' with a finite core σ.

Using this regularisation function, the vorticity field is now written as:

$$\vec{\omega}_\sigma(\vec{x}, t) = \xi_\sigma(\vec{x} - \vec{x}_i) \circledast \vec{\omega}(\vec{x}, t) = \sum_{i=1}^{N} \xi_\sigma(\vec{x} - \vec{x}_i)\vec{\alpha}_i(t), \qquad \ldots (8)$$

where $\vec{\omega}_\sigma(\vec{x}, t)$ is the regularised representation of the vorticity field and $\vec{\omega}(\vec{x}, t)$ is the vorticity field represented by the singular particles (Equation (5)).

There are many possibilities for the choice of the regularised function (regularised smoothing kernel). Examples of two and three-dimensional kernels can be found in Refs (68,69,70,65). In this work, Gaussian smoothing kernel, with order $r = 2$, was used. Gaussian smoothing regularisation function is a common choice for regularised vortex particles, as in Refs (58,59,71,72,73).

Detailed mathematical demonstration for the convergence and stability of the vorticity field represented by regularised vortex particles has been developed in many studies[69,67,74,75,76]. It has been shown that, for stability and accuracy, the particles need to satisfy the overlap criteria, which couples inter-particle distances and core sizes:

$$\frac{\sigma}{h} > 1, \qquad \ldots (9)$$

where h is the typical distance between neighbour particles.

2.4.4 Evolution equations

Substituting the vorticity representation, given by Equation (8), into the incompressible vorticity-velocity equation in Lagrangian form, Equation (4), results in the evolution equation for the strength of each particle i, as given by Equation (10). Also, vortex particles are considered fluid elements and, as so, travel with the local flow velocity (taking into account free-stream, velocity induced by particles, velocity induced by blades and any other influences in the velocity field), leading to the particle convection equation (Equation (11)).

$$\frac{D\vec{\alpha}_i}{dt} = [\vec{\alpha}_i \cdot \nabla]\vec{u} + \nu\nabla^2\vec{\alpha}_i \qquad \ldots (10)$$

$$\frac{d\vec{x}_i}{dt} = \vec{u}(\vec{x}_i, t). \qquad \ldots (11)$$

Equations (10) and (11) are the viscous vortex particle evolution equations, governing the update of particles strength and positions at each time step. The first term in the right-hand side of Equation (10), $[\vec{\alpha}_i \cdot \nabla]\vec{u}$, corresponds to the stretching effect, corresponding to vortex stretching and rotation due to the velocity field gradient. The second term in the right-hand side of that equation, $\nu\nabla^2\vec{\alpha}_i$, corresponds to the viscous diffusion, corresponding to the vorticity diffusion due to the viscous effects.

2.4.5 Generating new particles

After each time step, new particles are generated, satisfying the conservation of vorticity.

$$\vec{\Gamma}_{\text{wake}} = -\frac{d\vec{\Gamma}}{dt} + \vec{u}_b(\nabla \cdot \vec{\Gamma}) \qquad \ldots (12)$$

where $\vec{\Gamma}_{\text{wake}}$ is the circulation shed into the wake, $\vec{\Gamma}$ is the bound circulation and $\vec{u}_b$ is the resultant relative velocity between the airflow and the blade. The first term in the right-hand side of Equation (12) corresponds to the vorticity shed into the wake due to the time-varying circulation, called shed vorticity (associated with shedding particles). The second term corresponds to the vorticity released into the wake due to the gradient of circulation (in this case, the spanwise distribution of circulation) and is called trailing vorticity (associated with trailing particles).

2.5 Propeller inertial effects

The derivation of propeller inertia formulation is described in detail in previous work by the authors[33], and for completeness, it is summarised here.

The propeller is modeled as a rigid, massless rod with a distribution of concentrated masses. Also, it is assumed the propeller configuration is such that: (i) all blades have the same geometry and mass distribution, and (ii) the same angle between adjacent blades. Note that from (i) and (ii) one has:

$$\sum_{i=1}^{N_{\text{blades}}} \vec{r}_{\text{blade CG},i} = \vec{0}, \qquad \ldots (13)$$

where N_{blades} is the number of blades and $\vec{r}_{\text{blade CG},i}$ is the CG position of the i-th blade relative to the propeller hub, written in any desired frame. Both assumptions above are reasonable for most practical propellers.

Additionally, the following set of coordinate systems is considered (as presented in Fig. 2): (i) Inertial frame (I): as the name implies, a fixed inertial global frame; (ii) Body frame (B): a frame attached to the body, that may translate and rotate with relation to the inertial frame; (iii) Local beam frame (W): a frame attached to a structural beam node and it may translate and rotate in relation to the body frame due to elastic deformations; (iv) Propeller frame (P): a frame whose origin is attached at the propeller hub position and has no rotation or translation with relation to local frame W; (v) Blade frame (b): a frame that is attached to one of the propeller blades, has the same origin as the propeller frame, and rotates with relation to it with the propeller angular velocity.

Based on the coordinate systems defined, the position of one of the concentrated masses i defined with relation to the inertial frame (I) can be written in terms of the body frame (B) as:
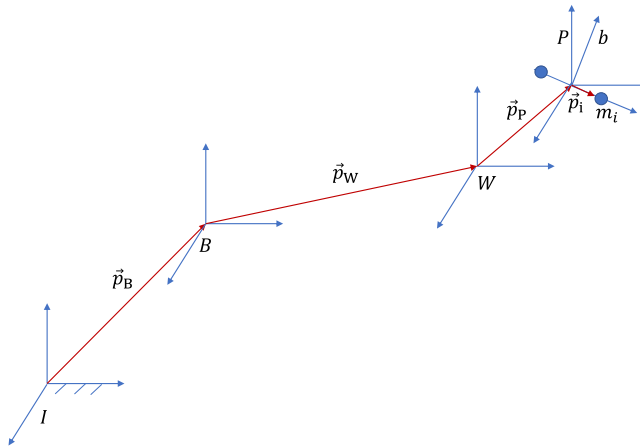
Figure 2. Representation of various reference systems used on modeling blade inertial effects. For simplicity, just one concentrated mass per blade is shown.

$$\vec{p}_{m_i} = \vec{p}_B + \vec{p}_W + \vec{p}_P + \vec{p}_i, \qquad \ldots (14)$$

where, as illustrated in Fig. 2, $\vec{p}_B$ is the position of the origin of the body frame with relation to the inertial frame, $\vec{p}_W$ is defined as the position of the origin of the local frame with relation to the body frame, $\vec{p}_P$ is the position of the origin of the propeller frame with relation to the local frame, and $\vec{p}_i$ is the position of the point mass i with relation to the propeller frame.

Recalling rigid-body dynamics theory, the time derivatives of a vector $\vec{r}$ expressed with respect to two different frames, (I) and (B), rotating with respect to each other is given by:

$$^I\dot{\vec{r}} = {}^B\dot{\vec{r}} + {}^I\vec{\omega}^B \times \vec{r}, \qquad \ldots (15)$$

where $^I\dot{\vec{r}}$ is the time derivative of $\vec{r}$ in frame I, $^B\dot{\vec{r}}$ is the time derivative of $\vec{r}$ with respect to B, and $^I\vec{\omega}^B$ is the angular velocity vector of B with relation to I.

The inertial force that each mass m_i transfers to the structure is:

$$\vec{F}_{m_i} = -m_i \, ^I\ddot{\vec{p}}_{m_i}. \qquad \ldots (16)$$

Applying Equation (15) into Equation (14) to calculate $^I\ddot{\vec{p}}_{m_i}$, substituting in Equation (16) and adding the contributions of all concentrated masses, one can find the following expression for the total force acting on the propeller hub due to inertial effects ($\vec{F}_{\text{hub}}$):

$$\begin{aligned}
\vec{F}_{\text{hub}} = \quad & m_p \, (\ddot{\vec{p}}_B + \ddot{\vec{p}}_W + \ddot{\vec{p}}_P + 2\,^I\vec{\omega}^B \times (\dot{\vec{p}}_B + \dot{\vec{p}}_W + \dot{\vec{p}}_P) \\
& + {}^I\dot{\vec{\omega}}^B \times (\vec{p}_B + \vec{p}_W + \vec{p}_P) + {}^I\vec{\omega}^B \times {}^I\vec{\omega}^B \times (\vec{p}_B + \vec{p}_W + \vec{p}_P)\,). \qquad \ldots (17)
\end{aligned}$$

Note that if one concentrates the mass m_p at the propeller hub location and follows a similar derivation, the same Equation (17) would be obtained. Then, as expected, the inertial forces acting on the propeller hub are equivalent to the force acting in a punctual mass m_p located at that location.

Now, consider the propeller inertial moments transferred to the body. The objective is to determine the moment due to the inertial forces acting on each rotating punctual mass transferred to the local node position, where the origin of the W frame is situated. The moment of those forces in relation to the origin of the W frame can be determined by:

$$\vec{M}_W = \vec{p}_P \times \vec{F}_{\text{hub}} + \sum_{k=1}^{N_{\text{seg}}} \sum_{i=1}^{N_{\text{blades}}} [\vec{p}_i \times \vec{F}_{mi}], \qquad \dots (18)$$

where N_{blades} and N_{seg} are the number of blades and blades segments, respectively and the index k is related to the radial position along the blade i.

Then, the moment transferred to the origin of the W frame due to the inertial forces from the rotating masses is equivalent to the moment with relation to the origin of the W frame due to a concentrated mass m_P at the propeller hub ($\vec{p}_P \times \vec{F}_{\text{hub}}$) plus a contribution due to the fact that masses are rotating around the hub ($\vec{M}_{\text{rot}} = \sum_{k=1}^{N_{\text{seg}}} \sum_{i=1}^{N_{\text{blades}}} [\vec{p}_i \times \vec{F}_{mi}]$).

Substituting the individual contributions $\vec{F}_{mi}$ of each concentrated mass (calculated as described previously), one can find:

$$\vec{M}_{\text{rot}} = \sum_{k=1}^{N_{\text{seg}}} \sum_{i=1}^{N_{\text{blades}}} -m_k [\vec{p}_{i,k} \times (\ddot{\vec{p}}_{i,k} + 2^I\vec{\omega}^B \times \dot{\vec{p}}_{i,k} \\ + {}^I\dot{\vec{\omega}}^B \times \vec{p}_{i,k} + {}^I\vec{\omega}^B \times {}^I\vec{\omega}^B \times \vec{p}_{i,k})], \qquad \dots (19)$$

with:

$$\dot{\vec{p}}_{i,k} = ({}^B\vec{\omega}^P + {}^P\vec{\omega}^b) \times \vec{p}_{i,k} \qquad \dots (20)$$

$$\ddot{\vec{p}}_{i,k} = {}^B\dot{\vec{\omega}}^P\, {}^b\vec{p}_{i,k} + ({}^B\vec{\omega}^P + {}^P\vec{\omega}^b) \\ \times ({}^B\vec{\omega}^P + {}^P\vec{\omega}^b) \times \vec{p}_{i,k}, \qquad \dots (21)$$

where m_k is the mass of a concentrated mass located at blade segment k, $\vec{p}_{i,k}$ is the position of the concentrated mass with relation to a frame attached to the propeller hub, ${}^I\vec{\omega}^B$ is the angular velocity of the body with relation to an inertial frame, ${}^B\vec{\omega}^P$ is the angular velocity of propeller frame with relation to body frame, and ${}^P\vec{\omega}^b$ is the angular velocity of blade frame with relation to propeller frame (given by propeller rotation per unit time). Also, all derivatives are defined in the body frame.

Then, the propeller inertial loads are incorporated by defining a concentrated mass m_p at each propeller hub and calculating an additional moment term given by Equations (19), (20) and (21).

2.6 Interface structure and aerodynamics

Since the structural model employs a 1D finite element representation, and the uVLM uses 2D non-planar grid, an interface between the two solvers is required to transfer loads and displacements.

Assuming rigid behavior in the chordwise direction (no change in local camber), the local beam coordinates and orientation given by the UM/NAST structural solver are converted to a non-planar panel grid by re-writing the camber line coordinates of each section along the span from aerofoil coordinates to body coordinates.
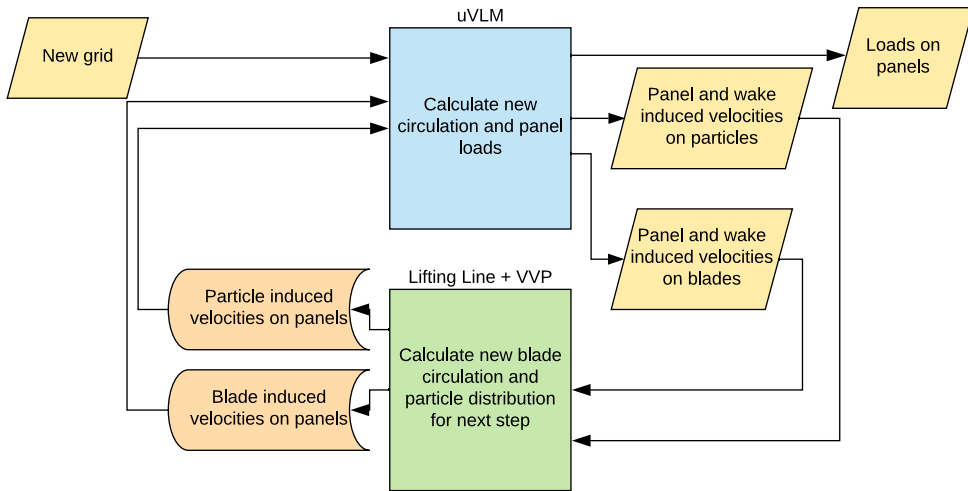
Figure 3. uVLM and propeller model integration approach.

The transfer of loads from panels to beam structural nodes is currently accomplished in two steps: (i) energy-consistent transfer of loads from the panels to the neighbouring points along the beam given by panel discretization (based on equivalence of virtual work between the forces at panels and forces transferred to beams) and (ii) linear transfer of loads from those points to the structural nodes, in case of different structural and aerodynamic spanwise discretisations. This approach is in accordance with the assumption of constant strains along each beam element.

2.7 Interface propeller and lifting surfaces aerodynamics

To integrate the uVLM for lifting surfaces with propeller modeling, the mutual influence between them needs to be taken into account. Figure 3 illustrates how the process of integration occurs.

At a given time step, the wing panel and wake panel circulations are updated by uVLM considering the induced velocity due to current particle distribution (calculated in the previous time step) and blade bound circulation. Then, based on the new wing and wake panel circulations, the new circulation of the blades are calculated, the existing particles have positions and strength updated, and new particles are generated, defining new particle distribution for the next time step. It is important to notice that the time step used in the propeller solver should be smaller than the propeller period divided by the number of blades. To not restrict the time step of the dynamic solver by the propeller solver requirements, one should consider the propeller time step smaller than the global dynamic solver time step. In this work, and unless otherwise stated, the propeller time step was half of the time step on the dynamic solver.

3.0 ALTERNATIVE APPROACH TO EXTRACT DYNAMIC INFORMATION

Traditionally, two main approaches are used to extract dynamic information (frequencies, damping, and modes) and perform a stability analysis of an aeroelastic system: frequency and time-domain methods. The frequency-domain methods are primarily developed for linear aeroelastic systems, as they assume the superposition of signals with different constant frequencies. Therefore, they are more suitable for problems with small deformations. Typical

methods for stability analysis based on frequency domain are the k method[77], p-k method[78] and p method[79].

For very flexible aircraft undergoing large deformations, however, strong nonlinearities can arise, and time-domain methods are usually preferred[80]. Examples of time-domain methods for stability analysis are reviewed in McNamara and Friedmann[81]: moving-block approach (MBA)[82], least squares curve-fitting method (LSCFM)[83] and system identification using the autoregressive moving-average (ARMA) model[84].

Even for linear systems, the complexity of the problem can make the use of frequency-domain techniques a cumbersome task, as the equations are not easily manipulated. In this case, time-domain simulations may also be preferred. In Silva[85], for example, the dynamic information of a linear transonic aeroelastic problem based on modal solutions is obtained by the system identification of CFD simulations.

3.1 Why an alternative approach?

In UM/NAST, the flutter solution is obtained based on the linearisation of the governing equations of the system. The model is first linearised about its trimmed condition, and then the dynamic information is extracted based on the eigendecomposition of the so-called state matrix A. This was developed by the original UM/NAST aerodynamic formulation, which used Peters' inflow theory.

Incorporating the UVLM aerodynamics for the lifting surfaces and LL/VVP formulation for the propellers in the UM/NAST linearised formulation would require an in-depth review of the linearisation formulation. Also, while the analytical expressions of Peters' inflow theory allow a direct coupling with the structural equations, the same is not the case for the UVLM and LL/VVP approaches, which are solved separately from the structural solver at each time step. This option was, then, out of the scope for the present work. Instead, an alternative approach for the stability analysis of VFA was proposed and applied. The procedure makes use of system identification combined with Proper Orthogonal Decomposition (POD) modes (Sys ID + POD) in order to reduce the number of degrees of freedom (outputs) of the problem. This is important, as the system identification is not well suited for a high number of outputs. Another advantage is that it can be applied to any time signal (e.g. experimental data), and a modal structural approach is not required (the method can be used for deformed configurations far from the undeformed condition).

3.2 Combining POD and Sys ID for stability analysis

In order to extract dynamic information (frequencies, damping, and modes) from the coupled aeroelastic-flight dynamics framework with propellers, it is first necessary to find a linearised mathematical representation of the system containing all the coupled structural, flight dynamics, lifting surfaces aerodynamics and propeller effects (inertial and aerodynamics).

One natural choice for this is to apply system identification and find a state-space representation of the global system. However, one difficulty in directly applying system identification in this context is that the VFA model often has a high number of degrees of freedom (the model considered later, for example, has more than 500 degrees of freedom), resulting in a high number of output states. However, system identification is not well suited for a high number of outputs, and the prediction performance is deteriorated.

One option to tackle this problem would be to write the output data as a function of a linear combination of the aircraft linear modes. This was done, for example, by Silva[85] and studies for aeroelastic problems involving small deformations. However, for a VFA, a representation of the deformed equilibrium state with linear modes is no longer adequate.
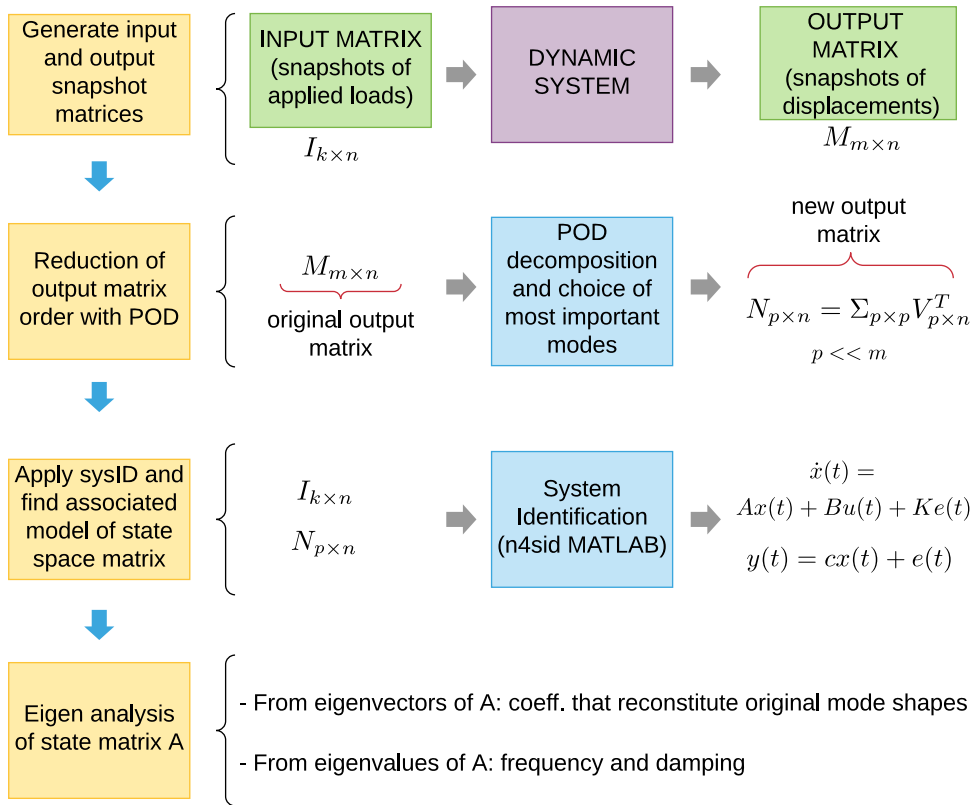
Figure 4. POD + Sys ID workflow.

Another alternative, used in this work, is to reduce the output matrix dimension by using POD modes. Then, instead of directly providing the output matrix containing the snapshots of displacements, the snapshots containing the coefficients of a much smaller number of POD modes are provided, and the original degrees of freedom are later recovered. This has the additional advantage of providing a better basis representation for an aircraft whose equilibrium state exhibits large deformation compared to the undeformed shape. Figure 4 illustrate how this combination of POD + Sys ID works.

First, the original data snapshots are collected by performing a time simulation disturbing the aircraft from its equilibrium condition. It is worthwhile to note that, for the extraction of dynamic information, it suffices to apply small disturbance around the deformed equilibrium condition, making possible the use of linear system identification approaches. Then, the input matrix consists of the snapshots of the values of loads (disturbances) applied. The original output matrix consists of the snapshots of the displacements (in x, y and z directions) of each structural nodes with relation to an initial equilibrium condition.

Next, the POD modes of the original output need to be determined and selected. For this, SVD is first applied to the original output matrix M:

$$M_{m\times n} = U_{m\times m}\,\Sigma_{m\times n}\,V_{n\times n}^{T} \qquad\qquad \ldots(22)$$

where m is the number of d.o.f., n is the number of snapshots, U and V are orthogonal matrices containing left-singular vectors and right-singular vectors of M, with the columns of

U corresponding to the POD modes, and Σ is a diagonal matrix of non-negative real number ordered in descending order. Also, the product $\Sigma_{m \times n} V_{n \times n}^T$ is associated with the coefficients of the POD modes which reconstitute the matrix M.

Usually, the first few POD modes are responsible for more than 99% of the trace of Matrix Σ. Reducing the number of POD modes to p, one obtains the new output matrix containing snapshots of the coefficients of the p POD modes which approximate the matrix M where $p << m$. For this, a reduced singular value decomposition representation of M can be found by using just the p POD modes selected as:

$$M_{m \times n} = U_{r,m \times p} \ \Sigma_{r,p \times p} \ V_{r,p \times n}^T \qquad \ldots (23)$$

The new reduced output matrix N to be provided to the system identification is then given by:

$$N_{p \times n} = \Sigma_{p \times p} \ V_{p \times n}^T \qquad \ldots (24)$$

Once the reduced output matrix is determined, an input-output based Sys ID is applied and an equivalent mathematical model given by the system of Equations (25) and (26) is determined:

$$\dot{x}(t) = A\,x(t) + B\,u(t) + K\,e(t) \qquad \ldots (25)$$

$$y(t) = C\,x(t) + K\,e(t), \qquad \ldots (26)$$

where A, B, C, and D are the estimated matrices of state space, K a matrix which accounts by disturbances, $u(t)$ is the input, $y(t)$ is the output and $x(t)$ is a vector with n_x states associated with this mathematical representation. The identification was performed using the tool n4sid available on Matlab and more details about the method can be found in Van Overschee and De Moor[86].

Finally, the dynamic information of the system can be found by the eigenvalue decomposition of matrix A, in Equation (25). As the state-space representation is in a continuous time domain, the frequencies and damping can be directly obtained from the eigenvalues λ_i of A, as:

$$freq = \frac{Re(\lambda_i)}{2\pi} \qquad \ldots (27)$$

$$damp = \frac{Imag(\lambda_i)}{2\pi}, \qquad \ldots (28)$$

where $Re(\lambda_i)$ and $Imag(\lambda_i)$ are the real and imaginary parts of λ_i, respectively.

From the eigenvectors of A, and remembering that they are related to coefficients of the chosen POD modes, the mode shapes can be obtained. Considering E as the matrix containing the eigenvectors of A and by Equation (26), the modes in terms of displacements at structural nodes can be recovered by:

$$N_{p \times n} = U_{r,m \times p} C_{p \times k} E_{k \times k} \qquad \ldots (29)$$

where k is the order chosen for the system identification method.

Table 1
Two-bladed APC 11X5.5E propeller parameters

Parameters	Values
Blade properties	APC 11X5.5 E
Aerofoil type	NACA 4412
Propeller mass	0.023kg
Number of blades	2
Blade discretization	4 segments
Time step	$T_P/10$
Sigma particles	0.0195

Due to nonlinearities, non-proportional damping, and possible noise, the modes obtained by the system identification can be complex. In Rainieri and Fabbrocino[87], a discussion of those complex modes from system identification is presented, and an approach, used in the present work, to convert them to real mode shapes was proposed. The mode shapes can be obtained by adding the real modes of displacements with the initial equilibrium condition.

Finally, it was observed that, for better accuracy, the number of frequencies determined should be no more than the number of POD modes selected.

4.0 NUMERICAL STUDIES

4.1 Simulation details

A verification of the POD combined with system identification (sys ID) is first performed by a purely structural case, and then the method is applied for the stability analysis of the aeroelastic cases. For these studies, two models are used: (i) the University of Michigan's X-HALE UAS[88] for the purely structural case and (ii) the University of Michigan's X-HALE UAS with an added tip mass of 0.5kg located 0.36m behind the wing trailing edge for the aeroelastic cases. This tip mass was added such that the model could present unstable aeroelastic behaviour in a range of velocities within the aircraft flight envelope. As shown in Fig. 5, the X-HALE has a wingspan of 6m with a 0.2-m chord, five pods along the wing, five tails, three fins and five electric motor-propeller combinations located in front of each pod at spanwise locations $y = -2, -1, 0, 1,$ and 2m. The wing is mounted with an incidence angle of 5 degrees. For the simulations, the propellers are located 20cm ahead and 2.8cm below of the wing leading edge, with a pitch angle of 5 degrees between the propeller axis and the X-HALE wing, as the wing has an incidence angle with respect to the pods. In order to reduce asymmetric loads, the propellers on the right wing have a different direction of rotation with relation to propellers at the left wing. A summary of the propeller parameters used here is presented in Table 1 and more details about the choice of blade discretisation and time step (based on a parametric study) and particle core radius (σ) can be found in Teixeira and Cesnik[33]. A cut-off distance of two radii after the end of the X-HALE vertical tails was applied to save computational cost. In the aeroelastic solver, a stiffness-proportional damping coefficient of 0.005s and a time step of 0.002s (for 6000RPM) and 0.0017 (for 7000RPM) were considered (with a sub-time step of half structural step). The dynamic viscosity is $\mu = 1.7855\ 10^5$N.s/m^2 and the air density is $\rho_\infty = 1.225$kg/m^3. For the aeroelastic cases, gravity effects are also considered.
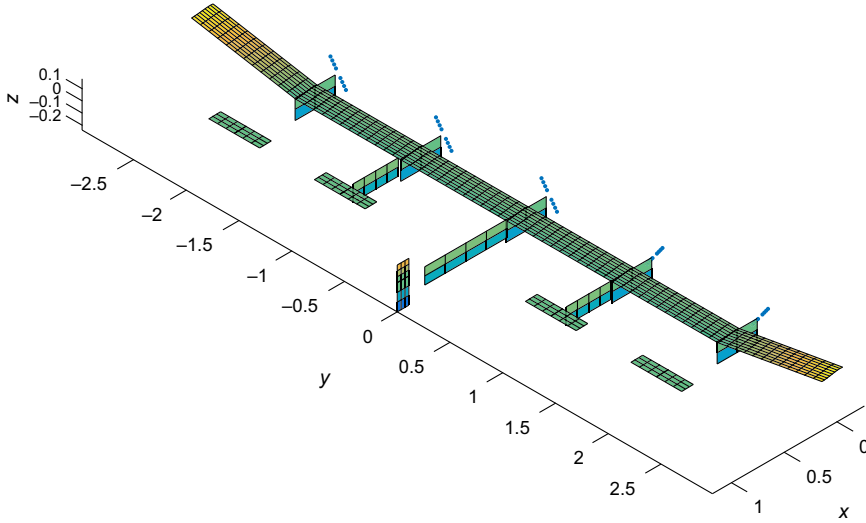
Figure 5. Undeformed panel model for the X-HALE UAS vehicle (units: meters).

4.2 Verifying POD + Sys ID for purely structural case

To verify the capability of the POD + Sys ID method to extract frequencies, damping, and modes based on the snapshots generated by the simulation of a VFA, a purely structural case was used, for which a reference from the UM/NAST modal solver was available about its undeformed shape. For the POD + Sys ID, a time simulation was performed for the clamped model from the undeformed configuration disturbed after 1.5s by a 5Nm torsion moment and a 1N step force in the vertical and chordwise direction, all applied at the right wing tip of the clamped model and chosen to excite different modes. The snapshots were then provided to the POD + Sys ID method, 5 POD modes were used (contributing for more than 99% of the snapshot energy), and an order of 18 was chosen for the system identification method based on the fitting quality of the POD coefficients. As the reference was for the undeformed, undamped case, no gravity or damping effects were included. Also, as the identification order of 18 provides nine frequencies, but just five POD modes are used (and up to five frequencies can be more accurately identified), the main frequencies were determined by choosing the five higher norms of the corresponding coefficients identified for the POD modes. Therefore the frequencies associated with the five columns of $C_{p \times k}E_{k \times k}$ with higher Euclidean norms were kept and shown in Fig. 6.

Table 2 presents the comparison between frequencies as well as a comparison of the corresponding modes by applying Model Assurance Criteria (MAC). For this purely structural case, one can see the method had an excellent agreement with the data calculated by the modal solver in UM/NAST with a maximum error in frequency prediction smaller than 2% and a MAC value of about 0.99 for all five modes.

4.3 Influence of the inclusion of aerodynamic and gyroscopic propeller effects on the aeroelastic stability

In order to check the additional influence of the propeller slipstream and gyroscopic effects, besides the influence of thrust, transient solutions for a clamped aeroelastic case were
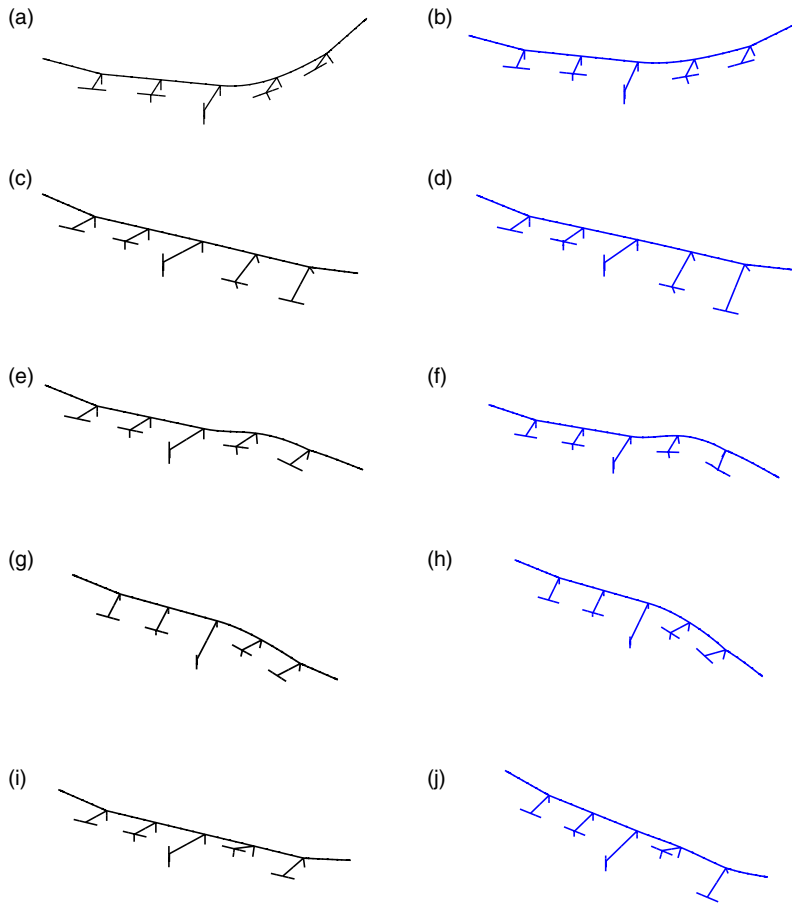
Figure 6. Comparison of mode shapes and natural frequencies for the X-HALE UAS vehicle about its undeformed configuration. (a) First bending (UM/NAST): 0.5943Hz. (b) First bending (POD + SysID): 0.5923Hz. (c) First torsion (UM/NAST): 2.5747Hz. (d) First torsion (POD + SysID): 2.5299Hz. (e) Second bending (UM/NAST): 3.6986Hz. (f) Second bending (POD + SysID): 3.6631Hz. (g) First in-plane bending (UM/NAST): 4.4491Hz. (h) First in-plane bending (POD + SysID): 4.4900Hz. (i) Second torsion (UM/NAST): 6.5696Hz. (j) Second torsion (POD + SysID): 6.5286Hz.

Table 2
Comparison of natural frequencies for purely structural case

UM/NAST (Hz)	POD + SysID (Hz)	Error (%)	MAC
0.5943	0.5923	−0.3422	0.9879
2.5747	2.5299	−1.7407	0.9896
3.6986	3.6631	−0.9596	0.9922
4.4491	4.4900	0.9195	0.9937
6.5696	6.5286	−0.6241	0.9980

conducted. Beginning from an equilibrium state and after 1.5s of simulation, a step perturbation of 5Nm in the torsional moment and a 1N step force in vertical and chordwise directions were applied. In this case, gravity and a stiffness-proportional damping coefficient of 0.005s were considered, to have a more realistic response. Three cases with different speeds: 12.5, 13 and 13.5m/s were simulated for a model with just thrust at the propeller location (equivalent to the thrust produced by the isolated propeller at each speed for the considered RPM) and a complete propeller model, including thrust (and other loads at hub), slipstream, and gyroscopic effects, with a rotation of 6000RPM.

First, the same set of parameters determined in the verification case was tried (five POD modes and Sys ID order of 18), but for the cases with aerodynamic and, for some of them, gyroscopic moment, the adjusting of the fifth POD coefficient using the same set of parameters for all cases was hard to get (especially for cases after the flutter boundary). Then, just four POD modes were considered (representing more than 99% of the snapshot energy), and an order of 18 was again included, improving the fitting of the first four POD coefficients. For the purely structural case, the effect of reducing the POD modes to four, keeping the same order for the Sys ID, was a reduction in the accuracy of higher frequencies. But the first four frequencies were kept with good accuracy (less than 2% error). Then, for the cases in this section, just four frequencies and modes are compared, corresponding to the most important modes for the system response. Also, the sensitivity of the results with the number of snapshots provided before the perturbation starts was found to be higher for cases with higher numerical perturbations, as in the cases after flutter. All cases use the same set of parameters, and it is expected that the results can capture frequency variations due to the different effects being modeled.

Figure 7 presents a comparison of the frequencies, dampings, and dynamic responses in terms of wing tip vertical and angular displacements for each simulated speed. From the dynamic responses, it is possible to see that for this model and propeller RPM, the flutter boundary is about 13m/s for both cases, i.e. thrust only, and including complete propeller modeling. However, as one can also observe from the dynamic responses, for all speeds increasing differences in phase arise between cases with thrust only and with all propeller effects for all speeds. For the same set of POD + Sys ID parameter choice, one can also note differences in frequencies and especially damping for modes farther away from the stability boundary. Considering that the variations of frequency and damping are captured, this indicates propellers can affect the dynamic response.

4.4 Influence of increasing propeller RPM

In order to investigate the effect of propeller RPM in the aeroelastic stability, a transient solution similar to the one presented in Fig. 7 was simulated for the clamped X-HALE model with tip masses at $v = 13$m/s and with a higher propeller rotation, 7000RPM. Increasing the propeller RPM with all other parameters constant means a stronger influence on the velocity flowfield behind the propeller plane of rotation, as well as a higher thrust and gyroscopic loads. It can be interpreted as the degree of propeller effects intensity, which could also be affected by other parameters like propeller mass, geometry, velocity flowfield, etc.

Figure 8 presents a comparison of the wing tip dynamic responses. Now, more noticeable differences can be observed in the stability behaviour; while the case with 6000RPM is yet stable (although close to flutter), the case with 7000RPM shows an unstable behaviour with increasing amplitudes, then a lower flutter speed. This destabilising effect with the increase in RPM is possibly related to the increase of dynamic pressure proportioned by the propeller
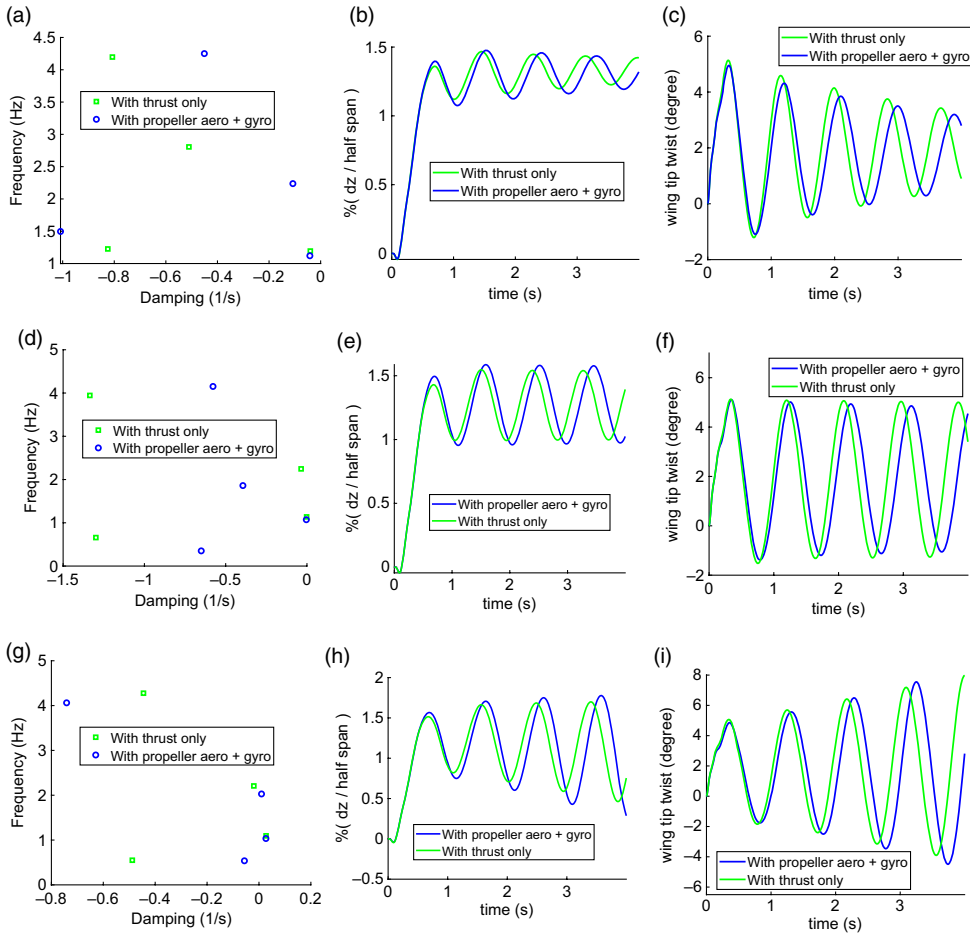
Figure 7. Frequencies, dampings, and response after perturbation with step loads of 5N in vertical and chordwise direction and 1Nm in torsion (6000RPM). (a) $v = 12.5$m/s. (b) $v = 12.5$m/s. (c) $v = 12.5$m/s. (d) $v = 13$m/s (e) $v = 13$m/s. (f) $v = 13$m/s. (g) $v = 13.5$m/s. (h) $v = 13.5$m/s. (i) $v = 13.5$m/s.

slipstream, causing higher lift forces for the same local angle-of-attack. This example indicates that depending on the intensity of propeller effects the influence on stability boundary can be more significant. Damping and frequency were not compared, as the same set of parameters used in $v = 13$m/s for 6000RPM do not provide a good fitting for the case of 7000RPM.

4.5 Contribution of different propeller effect components

Figure 9 compares the dynamic response as well as frequency and damping for the same disturbance, as in Fig. 8 for the clamped X-HALE model with tip masses at $v = 13$m/s. This case is already in the unstable regime. Due to more difficulties in find a common set of parameters with good fitting and in order to reduce the perturbation due to numerical noise, just three POD modes were incorporated (representing more than 97% of the snapshot energy), keeping the identification order as 18, and the snapshots were provided with 0.5s after beginning of perturbations.
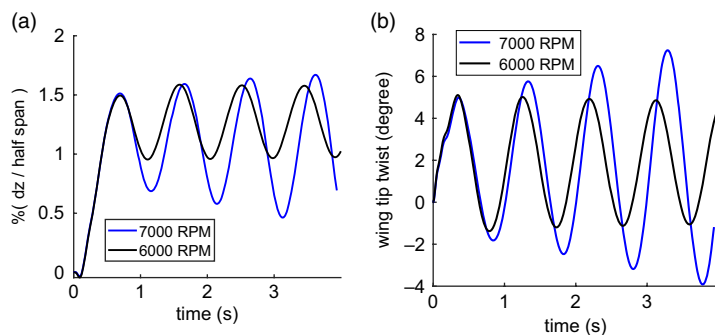
Figure 8. Wing tip response after perturbation with step loads of 5N in vertical and chordwise direction and 1Nm in torsion, including propeller aerodynamics and gyroscopic effects. (a) Tip vertical displacement. (b) Tip twist.
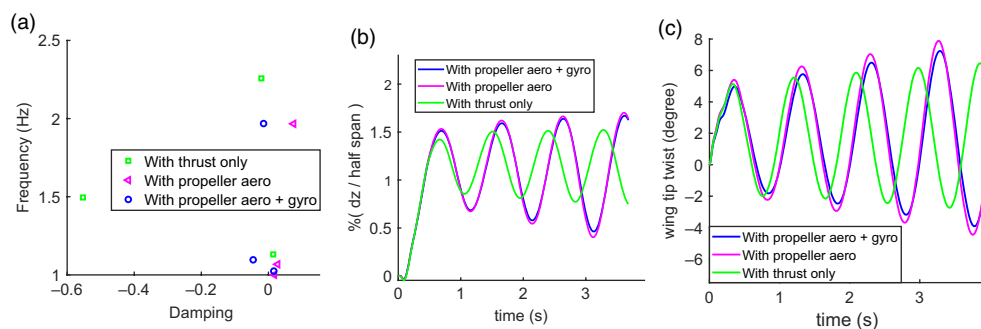

Figure 9. Frequencies, dampings, and response after perturbation with step loads of 5N in vertical and chordwise direction and 1Nm in torsion (7000RPM). (a) Root locus. (b) Wing tip vertical displacement. (c) Wing tip twist.

In order to observe the isolated propeller effect components (mainly thrust, slipstream, and gyroscopic moment), three different modelings of propeller effects are considered:

(i) with thrust only (equivalent to thrust produced by isolated propeller at $v = 13$m/s and 7000RPM);

(ii) with thrust (and other loads at the hub) and slipstream (propeller aero), and;

(iii) with thrust (and other loads at the hub), slipstream, and gyroscopic effects (propeller aero + gyro).

From the dynamic response, it is clear that the inclusion of propeller aerodynamic effects can cause a non-negligible difference in the aeroelastic stability, with the model including just thrust having a smoother amplitude increase, suggesting a higher flutter boundary. As previously commented, this destabilising effect may be related to the increased dynamic pressure due to the propeller slipstream, causing higher lift (and consequently higher structural deformations) for same freestream conditions. An increasing difference of phase with time is also noticeable between the case with just thrust and other two cases. The inclusion of gyroscopic effects causes negligible differences for vertical displacements but more visible differences in the amplitude of angular displacement, which is smaller for the case including gyroscopic

effects. This is in accordance with the root locus, where it is clear that the positive damping for the unstable modes in the case with slipstream and no gyroscopic effects is higher, suggesting the gyroscopic effect has a stabilising effect.

5.0 FINAL REMARKS

This work investigated the influence of propeller aerodynamics and gyroscopic effects on the aeroelastic stability of very flexible aircraft. For that, an enhanced aeroelastic framework with propellers developed in previous efforts by the authors[31,33] was applied to extract time-data snapshots of the clamped modified X-HALE UAS representing a HALE aircraft. A method based on POD plus system identification to extract frequencies, dampings and modes from the time-series data was successfully verified for a purely structural case for which a reference solution was available. The method was then used to analyse the effect of the propeller on the aeroelastic stability of the very flexible aircraft based on a set of generated snapshots. From the analysis of aeroelastic cases and the clamped model considered, it was observed that the presence of propeller aerodynamics and gyroscopic effects influences the values of damping and frequencies of some modes and can influence stability boundary. Moreover, an increase in phase delay and differences in amplitude in response to a perturbation close to flutter were shown as compared to the case with just thrust. A reduction of flutter boundary was found by an increase in propeller RPM. This destabilising effect may be associated with the impact of slipstream, increasing the dynamic pressure and local lift. Also, a slight stabilising effect due to the gyroscopic moment was noticed, suggesting this effect may be more important for cases with higher gyroscopic moment loads, i.e. higher RPM, and propeller mass. Finally, the method of POD plus system identification showed to be effective to extract frequencies, dampings, and modes for a purely structural case. Further investigations are necessary to make the method more robust for aeroelastic cases.

SUPPLEMENTARY MATERIAL

To view supplementary material for this article, please visit https://doi.org/10.1017/aer.2019.165.

ACKNOWLEDGEMENTS

REFERENCES

1. LANCHESTER, F.W. *The Flying Machine*, Wiley, 1917, New York.
2. HARRIS, R.G. Forces on a propeller due to sideslip, Tech Rep, Aeronautical Research Committee Reports and Memoranda No. 427, London, 1918.
3. GLAUERT, H. The stability derivatives of an airscrew, Tech Rep, Aeronautical Research Committee Reports and Memoranda No. 642, London, 1919.
4. GLAUERT, H. Airplane propellers. In *Aerodynamics Theory, Miscellaneous Airscrew Problems*, Vol. 4 div. L, Chapter XII, Secs. 5–6, Berlin, 1935, pp 351–359.

5. KATZOFF, S. Longitudinal stability and control with special reference to slipstream effects, *Tech Rep*, National Advisory Committee for Aeronautics, 1940.

6. RIBNER, H.S. Propellers in yaw, *Tech Rep*, National Advisory Committee for Aeronautics, 1945.

7. JAMISON, G.R. Flight Test Investigation of Propeller Effects on the Static Longitudinal Stability of the E-2C Airplane, Master's Thesis, The University of Tennessee, Knoxville, 2006.

8. GORAJ, Z.J. AND CICHOCKA, E. Influence of weak and strong gyroscopic effects on light aircraft dynamics, *Aircraft Eng Aerospace Tech*, 2016, **88**, (5), pp 613–622.

9. BOUQUET, T. Modelling the Propeller Slipstream Effect on the Longitudinal Stability and Control, Master's Thesis, Delft University of Technology, 2016.

10. REZAEIAN, A. Dynamic stability analysis of a propeller-wing wind tunnel model, Deutscher Luft- und Raumfahrtkongress, 2011, Bremen, Deutschland.

11. AN, S. Aeroelastic Design of a Lightweight Distributed Electric Propulsion Aircraft with Flutter and Strength Requirements, Master's Thesis, Georgia Institute of Technology, Atlanta, Georgia, 2015.

12. GURUSWAMY, G.P. Dynamic aeroelasticity of wings with tip propeller by using Navier–Stokes equations, *AIAA J*, 2019, **57**, (8), pp 3200–3205.

13. HODGES, D.H., PATIL, M.J. AND CHAE, S. Effect of thrust on bending-torsion flutter of wings, *J Aircraft*, 2002, **39**, (2), pp 371–376.

14. FELDT, W.T. AND HERRMANN, G. Bending-torsional flutter of a cantilevered wing containing a tip mass and subject to a transverse follower force, *J Franklin Inst*, 1974, **297**, (6), pp 467–468.

15. QUANLONG, C., JINGLONG, H. AND HAIWEI, Y. Effect of thrust engine on nonlinear flutter of wings, *J Vibroeng*, 2013, **15**, (4), pp 1731–1739.

16. RISO, C., DI VICENZO, F.G., RITTER, M., CESNIK, C.E.S. AND MASTRODDI, F. A fem-based approach for nonlinear aeroelastic trim of highly flexible aircraft, International Forum on Aeroelasticity and Structural Dynamics, IFASD 2017, Como, Italy, 25–28 June 2017.

17. SHEARER, C.M. AND CESNIK, C.E.S. Nonlinear flight dynamics of very flexible aircraft, *J Aircraft*, 2007, **44**, (5), pp 1528–1545.

18. SU, W. AND CESNIK, C.E.S. Dynamic response of highly flexible flying wings, *AIAA J*, 2011, **49**, (2), pp 324–339.

19. SU, W. AND CESNIK, C.E.S. Nonlinear aeroelasticity of a very flexible blended-wing-body aircraft, *J Aircraft*, 2010, **47**, (5), pp 1539–1553.

20. MURUA, J., PALACIOS, R. AND GRAHAM, J.M.R. Applications of the unsteady vortex-lattice method in aircraft aeroelasticity and flight dynamics, *Progress Aerospace Sci*, 2012, **55**, pp 46–72.

21. SIMPSON, R.J. AND PALACIOS, R. Numerical aspects of nonlinear flexible aircraft flight dynamics modeling, 54th AIAA/ASME/ASCE/AHS/ASC Structures, Structural Dynamics, and Materials Conference, American Institute of Aeronautics and Astronautics, 2013.

22. HESSE, H., PALACIOS, R. AND MURUA, J. Consistent structural linearization in flexible aircraft dynamics with large rigid-body motion, *AIAA J*, 2014, **52**, (3), pp 528–538.

23. DEL CARRE, A. AND PALACIOS, R. Low-altitude dynamics of very flexible aircraft, AIAA Scitech 2019 *Forum*, American Institute of Aeronautics and Astronautics, San Diego, California, 2019.

24. ASWING - MIT, http://web.mit.edu/drela/Public/web/aswing/, Accessed: 2019-08-05.

25. ASWING 5.97 User Guide, http://web.mit.edu/drela/Public/web/aswing/aswing_doc.txt, Accessed: 2019-08-05.

26. ASWING 5.99 Technical Description, https://pdfs.semanticscholar.org/c919/59501949e68b0fd1005b097e1e4db2952eb0.pdf, Accessed: 2019-08-05.

27. CHANG, C.S. Vibration and Aeroelastic Analysis of Highly Flexible HALE Aircraft. PhD Thesis, Georgia Institute of Technology, USA, 2006.

28. MARDANPOUR, P. AND HODGES, D.H. On the importance of nonlinear aeroelasticity and energy effciency in design of flying wing aircraft, *Adv Aerospace Eng*, 2015, pp 1–11.

29. RITTER, M., CESNIK, C.E.S. AND KRUGER, W.R. An enhanced modal approach for large deformation modeling of wing-like structures, AIAA Science and Technology Forum and Exposition (SciTech2015), 56th AIAA/ASCE/AHS/ASC Structures, Structural Dynamics, and Materials Conference, AIAA Paper 2015-0176, January 2015.

30. RITTER, M., JONES, J. AND CESNIK, C.E.S. Enhanced modal approach for free-flight nonlinear aeroelastic simulation of very flexible aircraft, AIAA Science and Technology Forum and Exposition (SciTech2016), 15th Dynamics Specialists Conference, AIAA Paper 2016-1794, January 2016.

31. TEIXEIRA, P.C. AND CESNIK, C.E.S. Inclusion of propeller effects on aeroelastic behavior of very flexible aircraft, International Forum on Aeroelasticity and Structural Dynamics, IFASD 2017, Como, Italy, 25–28 June 2017.

32. TEIXEIRA, P.C. AND CESNIK, C.E.S. Propeller effects on the dynamic response of hale aircraft, AIAA/ASCE/AHS/ASC Structures, Structural Dynamics, and Materials Conference, AIAA SciTech Forum, 2018, Kissimmee, Florida, 8–12 January 2018.

33. TEIXEIRA, P.C. AND CESNIK, C.E.S. Propeller effects on the response of high-altitude longendurance aircraft, *AIAA J*, **57**, (10), pp 4328–4342.

34. TEIXEIRA, P.C. Propeller Effects on Very Flexible Aircraft, PhD Thesis, University of Michigan, USA, 2019.

35. SU, W. AND CESNIK, C.E.S. Strain-based geometrically nonlinear beam formulation for modeling very flexible aircraft, *Int J Solids Struct*, 2011, **48**, (16–17), pp 2349–2360.

36. PETERS, D.A. AND JOHNSON, M.J. Finite-state airloads for deformable airfoils on fixed and rotating wings. *American Soc Mechan Eng*, 1994, **44**, pp 1–28.

37. PETERS, D.A. AND CAO, W. Finite state induced flow models, part 1: two-dimensional thin airfoil, *J Aircraft*, 1995, 32, (2), pp 313–322.

38. RITTER, M., TEIXEIRA, P.C. AND CESNIK, C.E.S. Comparison of nonlinear aeroelastic methods for maneuver simulation of very flexible aircraft, 2018 AIAA/ASCE/AHS/ASC Structures, Structural Dynamics, and Materials Conference, AIAA SciTech Forum. AIAA Paper 2018–1953, January 2018.

39. KIMA, D., LEEB, J.S., LEEB, J.H. AND HANB, J. An aeroelastic analysis of a flexible flapping wing using modified strip theory, SPIE 15th Annual Symposium Smart Structures and Materials, 2008.

40. PATIL, M.J., HODGES, D.H. AND CESNIK, C.E.S. Nonlinear aeroelastic analysis of complete aircraft in subsonic flow, *J Aircraft*, 2000, **37**, (5), pp 753–760.

41. GEORGIOU, G., VIO, G.A. AND COOPER, J.E. Aeroelastic tailoring and scaling using bacterial foraging optimisation, *Struct Multidiscipl Opt*, 2014, **50**, (1), pp 81–99.

42. WEISSHAAR, T.A. Aeroelastic tailoring of forward swept composite wings, *J Aircraft*, 1981, **18**, (8), pp 669–676.

43. RITTER, M.R. An Extended Modal Approach for Nonlinear Aeroelastic Simulations of Highly Flexible Aircraft *Structures*, PhD Thesis, Technischen Universitt Berlin, Berlin, 2018.

44. HUANG, Y. AND SU, W. Linearization and analytical aerodynamic sensitivity of unsteady vortex-lattice aerodynamics, AIAA Scitech 2019 Forum, 2019.

45. del CARRE, A., TEIXEIRA, P.C., PALACIOS, R. AND CESNIK, C.E.S. Nonlinear response of a very flexible aircraft under lateral gust, International Forum on Aeroelasticity and Structural Dynamics, IFASD, Savannah, Georgia, USA, June 2019.

46. CHAO, Y., LiBo, W., ChangChuan, X. AND YI, L. Aeroelastic trim and flight loads analysis of flexible aircraft with large deformations, *Sci China Tech Sci*, 2012, **55**, (10), pp 2700–2711.

47. XIE, C., WANG, L., YANG, C. AND LIU, Y. Static aeroelastic analysis of very flexible wings based on non-planar vortex lattice method, *Chinese J Aeronautics*, 2013, **26**, (3), pp 514–521.

48. GUIMARAES NETO, A.B.G. Approximation of aerodynamic geometrical nonlinearities in aircraft with high-aspect-ratio wings, International Forum on Aeroelasticity and Structural Dynamics, IFASD, Savannah, Georgia, USA, June 2019.

49. HESSE, H. AND PALACIOS, R. Reduced-order aeroelastic models for dynamics of maneuvering flexible aircraft, *AIAA J*, 2014, **52**, (8), pp 1717–1732.

50. NGUYEN, N., REYNOLDS, K., TRINH, K. AND FROST, S. Coupled aeroelastic vortex lattice modeling of flexible aircraft, 29th AIAA Applied Aerodynamics Conference, 2012.

51. JAMES, R.M. On the remarkable accuracy of the vortex lattice method, *Comput Methods Appl Mech*, 1972, **1**, (1), pp 59–79.

52. RITTER, M., DILLINGER, J. AND MEDDAIKAR, Y.M. Static and dynamic aeroelastic validation of a flexible forward swept composite wing, AIAA SciTech, 58th AIAA/ASCE/AHS/ASC Structures, Structural Dynamics, and Materials Conference, Grapevine, Texas, January 2017.

53. FALKNER, V.M. The scope and accuracy of vortex lattice theory, Tech Rep, Reports and Memoranda 2740, London, 1949.

54. MURUA, J., PALACIOS, R. AND MICHAEL, R.G.J. Modeling of nonlinear flexible aircraft dynamics including free-wake effects, AIAA Atmospheric Flight Mechanics Conference, Toronto, Ontario, Canada, 2–5 August 2010. DOI: 10.2514/6.2010-8226

55. MURUA, J., PALACIOS, R. AND MICHAEL, R.G.J. Assessment of wake-tail interference effects on the dynamics of flexible aircraft, *AIAA Journal*, 2012, **50**, (7), pp 1575–1585.

56. Abedi, H., Davidson, L. and Voutsinas, S. Vortex method application for aerodynamic loads on rotor blades, EWEA 2013: Europe's Premier Wind Energy Event, 2013, Vienna, Austria, 4–7 February 2013.

57. Tan, J., Sun, Y. and Barakos, G.N. Unsteady loads for coaxial rotors in forward flight computed using a vortex particle method, *Aeronautical J*, 2018, **122**, (1251), pp 693–714.

58. Singh, P. and Friedmann, P.P. Application of vortex methods to coaxial rotor wake and load calculations in hover, *J Aircraft*, 2017, **55**, (1), pp 373–381.

59. He, C. and Zhao, J. Modeling rotor wake dynamics with viscous vortex particle method, *AIAA Journal*, 2009, **47**, (4), pp 902–915.

60. Singh, P. and Friedmann, P.P. Dynamic stall modeling using viscous vortex particle method for coaxial rotors, Vertical Flight Society 75th Annual Forum and Technology Display, Philadelphia, Pennsylvania, 13–16 May 2019.

61. Calabretta, J.S. A Three Dimensional Vortex Particle-panel Code for Modeling Propellerairframe Interaction, Master's Thesis, California Polytechnic State University, San Luis Obispo, 2010.

62. Willis, D.J. An Unsteady, Accelerated, High Order Panel Method with Vortex Particle Wakes, PhD Thesis, Massachusetts Institute of Technology, Cambridge, 2006.

63. Thepvongs, S., Cesnik, C.E.S. and Voutsinas, S.G. Aeroelastic and acoustic analysis for active twist rotors, 31st European Rotorcraft *Forum*, 2005, Florence, Italy, 13–15 September 2005.

64. Alvarez, E.J. and Ning, A. Development of a vortex particle code for the modeling of a wake interaction in distributed propulsion, AIAA Aviation *Forum*, 25–29 June 2018, Atlanta, Georgia.

65. Winckelmans, G.S. and Leonard, A. Contributions to vortex particle methods for the computation of three-dimensional incompressible unsteady flows, *J Comput Phys*, 1993, **109**, (2), pp 247–273.

66. Speck, R. *Generalized Algebraic Kernels and Multipole Expansions for Massively Parallel Vortex Particle Methods*. IAS *Series* Volume **7**. Schriften des Forschungszentrums Jlich, 2011.

67. Beale, J.T. and Majda, A. Vortex methods. I - Convergence in three dimensions. II - Higher order accuracy in two and three dimensions, *Math Comput*, 1982, **39**, pp 1–52.

68. Beale, J. and Majda, A. High order accurate vortex methods with explicit velocity kernels, *J Comput Phys*, 1985, **58**, (2), pp 188–208.

69. Hald, O. and Del Prete, V.M. Convergence of vortex methods for Euler's equations, *Math Comput*, 1978, **32**, (143), pp 791–809.

70. Nordmark, H.O. Rezoning for higher order vortex methods, *J Comput Phys*, 1991, **97**, (2), pp 366–397.

71. Rajmohan, N., Zhao, J. and He, C. A coupled vortex particle/cfd methodology for studying coaxial rotor configurations, Fifth Decennial AHS Aeromechanics Specialists' Conference, San Francisco, CA, 22–24 January 2014.

72. Zhao, J. and He, C. A viscous vortex particle model for rotor wake and interference analysis, Journal of the American Helicopter Society, 2010, 55, pp 12007.

73. Zhao, J. and He, C. Real-time simulation of coaxial rotor configurations with combined finite state dynamic wake and vpm, Vol. 3, 2014.

74. Cottet, G.H. PhD Thesis, Universit Paris 6, Paris, 1982.

75. Anderson, C. and Greengard, C. On vortex methods, *SIAM J Numer Anal*, 1985, **22**, (3), pp 413–440.

76. Beale, J.T. A convergent 3-d vortex method with grid-free stretching, *Math Comput*, 1986, **46**, (174), pp 401–424.

77. Bisplinghoff, R.L. and Ashley, H. *Principles of Aeroelasticity*, John Wiley, 1962, New York.

78. Hassig, H.J. An approximate true damping solution of the flutter equation by determinant iteration, *J Aircraft*, 1971, **8**, (11), pp 885–889.

79. Abel, I. An analytical technique for predicting the characteristics of a flexible wing equipped with an active flutter-suppression system and comparison with wind-tunnel data, Tech Rep, NASA-TP-1367, L-12567, 1979.

80. Hallissy, B. and Cesnik, C.E.S. High-fidelity aeroelastic analysis of very flexible aircraft, 52nd AIAA/ASME/ASCE/AHS/ASC Structures, Structural Dynamics and Materials Conference, 2011.

81. McNamara, J.J. and Friedmann, P.P. Flutter boundary identification for time-domain computational aeroelasticity, *AIAA J*, 2007, **45**, (7), pp 1546–1555.

82. HAMMOND, C.E. AND DOGGET, J.R.V. An analytical technique for predicting the characteristics of a flexible wing equipped with an active flutter-suppression system and comparison with wind-tunnel data, Tech Rep, NASA Scientific and Technical Information Offce, Washington, 1975.

83. BENNETT, R.G. AND DESMARAIS, R. Curve-fitting of aeroelastic transient response data with exponential functions, Tech Rep, NASA SP-415, 1975.

84. ONODA, J. Estimation of dynamic characteristics of a wing from the random response to turbulence, *J Japan Soc Aeronaut Space Sci*, 1978, **26**, (299), pp 649–656.

85. SILVA, W.A. AEROM: NASA's unsteady aerodynamic and aeroelastic reduced-order modeling software, *Aerospace*, 2018, **5**, (2), pp 1–18.

86. VAN OVERSCHEE, P. AND DE MOOR, B. N4sid: subspace algorithms for the identification of combined deterministic-stochastic systems, *Automatica*, 1963, **11**, (2), pp 431–441.

87. RAINIERE, C. AND FABBROCINO, G. *Operational Modal Analysis of Civil Engineering Structures*, Spring-Verlag, 2014, *New York*, pp 182–183.

88. CESNIK, C.E.S., SENATORE, P.J., SU, W., ATKINS, E.M. AND SHEARER, C.M. X-hale: a very flexible unmanned aerial vehicle for nonlinear aeroelastic tests, *AIAA Journal*, 2012, **50**, (12), pp 2820–2833.